

## Supplementary Information

### Memory-effect-induced Electrochemical Oscillation of Al-doped

### Li<sub>4</sub>Ti<sub>5</sub>O<sub>12</sub> composite in Li-ion batteries

Liao Zhang<sup>a</sup>, Yanyu Qu<sup>a</sup>, Jiangtao Huang<sup>a</sup>, Xiang Feng<sup>a</sup>, De Li<sup>\*a,b</sup>, Yong Chen<sup>\*a,c</sup>

<sup>a</sup> State Key Laboratory on Marine Resource Utilization in South China Sea, Hainan Provincial Key Laboratory of Research on Utilization of Si-Zr-Ti Resources, College of Materials Science and Chemical Engineering, Hainan University, Haikou, China.

<sup>b</sup> National Laboratory of Solid State Microstructures, Nanjing University, Nanjing, China.

<sup>c</sup> Key Laboratory of Advanced Energy Materials Chemistry (Ministry of Education), Nankai University, Tianjin, China.

\*Corresponding Author

E-mail: lidenju@sina.com (D. Li); ychen2002@163.com (Y. Chen);

Tel.: +86-898-66277929 (Y. Chen)

**30th July 2019**

**Note added after first publication:** The <sup>27</sup>Al MAS NMR spectra in the original version of the Supplementary Information published on 2nd January 2019 was incorrect. This revised version includes the corrected data in Fig. S3. A correction to the original article was also published with further details (DOI: 10.1039/C9CC90335F).

## Experimental Section

### Synthesis

Pristine  $\text{Li}_4\text{Ti}_5\text{O}_{12}$  (LTO) was purchased from Ishihara Sangyo Kaisha, Ltd. and nano- $\text{Al}_2\text{O}_3$  (mean particle size: 22.2–47.7 nm) was supplied by Nanophase Technologies Corp. (NanoTek®). The Al-doped  $\text{Li}_4\text{Ti}_5\text{O}_{12}$  composite (ALTO) was synthesized by a solid-state reaction by using LTO and nano- $\text{Al}_2\text{O}_3$  with a ratio of 4:1, in which the precursors were ground thoroughly and then calcined at 800 °C for 15 h in air.

### Structural Characterization

The morphology was characterized with scanning electron microscopy (SEM, Phenom ProX). The X-ray diffractions (XRD) of LTO and ALTO were collected by using a Bruker D8 Advance diffractometer with filtered Cu-K $\alpha$  radiation. Raman spectra were collected by using a Raman spectrometer (Thermo Fisher Scientific DXRxi) with a laser wavelength of 532 nm. The chemical valence state of elements was investigated by using X-ray photoelectron spectroscopy (XPS, Axis Supra) with a focused monochromatized Al K $\alpha$  radiation (1486.6 eV). The solid-state  $^{27}\text{Al}$  MAS NMR experiments were performed on a JNM-ECZR 600MHz (14.09 T) spectrometer operating at a frequency of 156.385 MHz. The rotating frequency used was 15 kHz; a standard 8 mm probe head (JNM) was employed. Powdered sample was packed into a zirconia rotor (2mm in diameter). The spectra were recorded with a single pulse excitation using a 90° pulse of 23  $\mu\text{s}$  and a recycle delay of 10 s.  $^{27}\text{Al}$  chemical shifts were referenced using 1 M aqueous solution of  $\text{Al}(\text{NO}_3)_3$  as an external reference (0 ppm).

### Electrochemical measurements

Electrochemical measurements were carried out using coin cells (CR2032). The counter electrode of lithium metal was separated from the working electrode by a Celgard 2400 porous polypropylene film, and the electrolyte used was 1 M  $\text{LiClO}_4$  in ethylene carbonate/diethyl carbonate (EC/DEC with a volume ratio of 1:1). The working electrode, containing 42.5 wt% active material (ALTO), 42.5 wt%

conductivity agent (acetylene black) and 15 wt% binder (polytetrafluoroethylene, PTFE), was firmly sandwiched between two carbon papers with a mass loading of *ca.* 3mg cm<sup>-2</sup>. Here, 42.5 wt.% acetylene black was added to enhance the electronic conductivity. After drying all components, the cells were assembled in an argon-filled glove box. The electrochemical measurements were conducted with a battery charge/discharge system from Hokuto Denko Corp. and a CellTest 8 channel potentiostat–galvanostat (Solartron 1470E). By using a potentiostat–galvanostat with an impedance analyzer (Solartron 1287 and 1260A), the electrochemical impedance spectroscopy (EIS) was collected from 10<sup>6</sup> Hz to 10<sup>-2</sup> Hz.

### **In situ XRD characterization**

As described in our previous paper, a  $\Phi$ 14mm hole was drilled on the bottom case of a normal 2032 coin cell for the in situ XRD measurement, and an Al foil as an X-ray window was firmly attached to the bottom case with Thermo-Bond Film TBF615-4mil from the 3M Company.<sup>1</sup> The counter electrode was a lithium foil, the glass fiber was used as a separator, and the electrolyte was 1M LiClO<sub>4</sub> in ethylene carbonate/dimethyl carbonate/ethyl methyl carbonate (EC/DMC/EMC with a volume ratio of 1:1:1). All the components were assembled in an argon-filled glove box. The in situ XRD measurement was conducted by using a Bruker D8 Advance diffractometer with Cu K $\alpha$  radiation. The data were collected every one hour and the XRD patterns were calibrated with the aluminum peak. Simultaneously, the electrochemical measurements were conducted on an Autolab electrochemical instrument with potentiostatic at 2 V for 1 h, discharging to 1.2 V at 0.1 C, potentiostatic at 1.2 V for 1 h, charging to 2 V at 0.1 C.

## Results and discussion

### XPS Characterization

To obtain detailed information about elemental valence of ALTO, the X-ray photoelectron spectroscopy (XPS) results are shown in Fig.S1. The binding energy of all XPS spectra were calibrated with C 1s = 284.8eV. From the Ti 2p spectrum of ALTO (Fig.S1b), two characteristic peaks at binding energies of 458.6 and 464.3 eV belong to typical Ti 2p<sub>3/2</sub> peak and Ti 2p<sub>1/2</sub> peak of Ti<sup>4+</sup>,<sup>2</sup> and no other peaks of Ti ion in different valence such as Ti<sup>3+</sup> or Ti<sup>2+</sup> are observed, which indicates that Ti ions could be most probably oxidized to Ti<sup>4+</sup> as ALTO is calcined in the air environment. As shown in Fig.S1c, the Al 2p core peak appears at 74.5 eV assigned to Al<sup>3+</sup>,<sup>3,4</sup> which possesses the ionic bonding characteristic.<sup>5</sup> Typical peaks of O 1s is shown in Fig.S1d. The O 1s peak at about 529.6 eV represents the Ti-O bond in LTO or TiO<sub>2</sub>,<sup>6</sup> the Al-O bond is at about 530.6 eV, and the peak at about 531.7 eV is assigned to the chemisorbed oxygen on the surface of crystallites.<sup>7</sup>

### <sup>27</sup>Al MAS NMR Characterization

The <sup>27</sup>Al MAS NMR experiments were conducted to determine the occupied site of Al ions in the lattice structure of Li<sub>4</sub>Ti<sub>5</sub>O<sub>12</sub>. In the <sup>27</sup>Al MAS NMR spectra of Al-doped Li<sub>4</sub>Ti<sub>5</sub>O<sub>12</sub> (ALTO-2, 2 wt% Al<sub>2</sub>O<sub>3</sub>) (Fig.S3a) and ALTO (20 wt% Al<sub>2</sub>O<sub>3</sub>) (Fig.S3b), isotropic peaks at around 74 and 17 ppm were assigned to tetrahedral (AlO<sub>4</sub>) and octahedral (AlO<sub>6</sub>) coordinated Al ions, respectively.<sup>8-10</sup> The Al ions distribute on only 8a site in the lattice structure of ALTO-2. Due to some Al<sub>2</sub>O<sub>3</sub> impurity in ALTO (20 wt% Al<sub>2</sub>O<sub>3</sub>), there are a few Al ions in the octahedron (AlO<sub>6</sub>). As a whole result, the Al ions occupy only 8a site in the lattice structure of Li<sub>4</sub>Ti<sub>5</sub>O<sub>12</sub>.

### Electrochemical Results and Discussion

Figure S4 shows the electrochemical oscillation of two Al-doped Li<sub>4</sub>Ti<sub>5</sub>O<sub>12</sub> composites. When the amount of Al<sub>2</sub>O<sub>3</sub> is 20 wt%, the memory effect and the electrochemical oscillation occur simultaneously (Fig.S4b). However, when the amount of Al<sub>2</sub>O<sub>3</sub> is 10 wt%, there is only memory effect on the charging curve, but no electrochemical oscillation (Fig.S4a). In our previous report,<sup>11</sup> when the amount of

$\text{Al}_2\text{O}_3$  was below 10 wt %, the memory effect existed in Al-doped  $\text{Li}_4\text{Ti}_5\text{O}_{12}$  electrode but no electrochemical oscillation.

As shown in Fig.S5a, the memory effect is confirmed as an important condition for the appearance of electrochemical oscillation by adjusting the memory-writing step. As we known, when discharging at a high cutoff, the phase transition is between the  $\alpha$  (delithiated) and  $\beta$  (lithiated) phases. After further discharging to a low cutoff, the  $\beta$  phase will be evolved with poor electrochemical kinetics.<sup>11</sup> Here, the phase transition of memory effect can be described by a schematic diagram, as shown in Fig.S5b. In the first cycle, when the electrode was discharged to 1.2 V and potentiostatic for 2h, the  $\alpha$  phase was transformed into the  $\beta_2$  phase, a part of which was transformed back in the subsequent charging process. In the second cycle, when the electrode was discharged to 1.2 V and potentiostatic for 2 h, the  $\beta_2$  phase was transformed into the  $\beta_3$  phase, and the  $\alpha$  phase was transformed into the  $\beta_2$  phase, a part of which was transformed back in the subsequent charging process. In the third cycle, when the electrode was discharged to 1.2 V, the  $\alpha$ ,  $\beta_2$  and  $\beta_3$  phases are transformed into  $\beta_2$ ,  $\beta_3$ ,  $\beta_4$  phases, respectively, and then a part of  $\beta_2$  phase was transformed back in the subsequent charging process. Here, it was different of the  $\beta_2$  phases with and without potentiostatic for 2h, while we considered them as the same for simplicity. In the last cycle, when the electrode was discharged to 1.5V, the  $\beta_2$ ,  $\beta_3$  and  $\beta_4$  phases would not change and the  $\alpha$  phase was transformed into  $\beta_1$  phase. Owing to the different electrochemical kinetics, a incremental potential was necessary to convert the  $\beta_1$ ,  $\beta_2$ ,  $\beta_3$  and  $\beta_4$  phase into the  $\alpha$  phase during the memory-releasing step of charging to 2.0 V, which exhibited as a four-stepped plateau.

To identify the difference between the electrode ALTO with different discharging cutoffs, the electrode is discharged to 1.5V (1.2V) and charge to 2V, and the EIS spectra were measured point by point in the two-phase region during the (dis)charging process, as shown in Fig.S7a and S7d. The Nyquist plots are presented in Fig.S7b, c, e and f for the charging and discharging processes, respectively. Fig.S8a shows a Randle equivalent circuit to simulate the impedance spectra of ALTO electrode. In the Randle equivalent circuit, the  $R_1$  is an ohmic resistance related to the transport of lithium ions

through electrolyte. The  $R_2$  and  $CPE_1$  are associated with lithium ions passing through the solid–electrolyte interphase (SEI) film. The  $R_3$  and  $CPE_2$  are associated with the charge transfer process and the  $R_3$  represents the charge-transfer resistance ( $R_{ct}$ ). The  $CPE_3$  is used to fit a tilted line related to the diffusion process of lithium ions in the active material. The impedance of CPE ( $Z_{CPE}$ ) is defined by the CPE index  $n$  (CPE-P) and CPE constant  $T$  (CPE-T) as follows :

$$Z_{CPE} = \frac{1}{T(j\omega)^n}$$

where  $T$  is a CPE constant with unit of  $\Omega^{-1} S^n cm^{-2}$ ,  $j^2 = -1$ ,  $\omega$  is the angular frequency and  $n$  is the coefficient related to the deviation between real capacitance and pure capacitance with values between 1 and 0. CPE can represent resistance ( $n = 0$ ,  $Z_{CPE} = R$ ), capacitance ( $n = 1$ ,  $Z_{CPE} = C$ ), or Warburg impedance ( $n = 0.5$ ,  $Z_{CPE} = W$ ) Respectively.

The simulated  $R_{ct}(R_3)$ , CPE-P ( $n$ ) and CPE-T ( $T$ ) values of  $CPE_3$  are presented in Fig.S8. Before discharging, the relaxation time for the battery was not the same, so the  $R_{ct}$ , CPE-P and CPE-T values of discharging process were slightly different. During discharging, these values gradually became consistent (Fig.S8b, d and f). During the charging process, the  $R_{ct}$  values barely changed with two discharging cutoffs (Fig.S8c), the CPE-P ( $n$ ) values with the discharging cutoff of 1.2V was obviously larger than that of 1.5V (Fig.S8e). And the CPE-T ( $T$ ) value rose slowly for the discharging cutoff of 1.5V, while the CPE-T ( $T$ ) value for the discharging cutoff of 1.2V rose sharply at the beginning of charging process (Fig.S8g). Thereby, during the charging process, the electrochemical kinetics were not the same for the ALTO electrode from different discharging cutoffs.

## Supplementary Figures

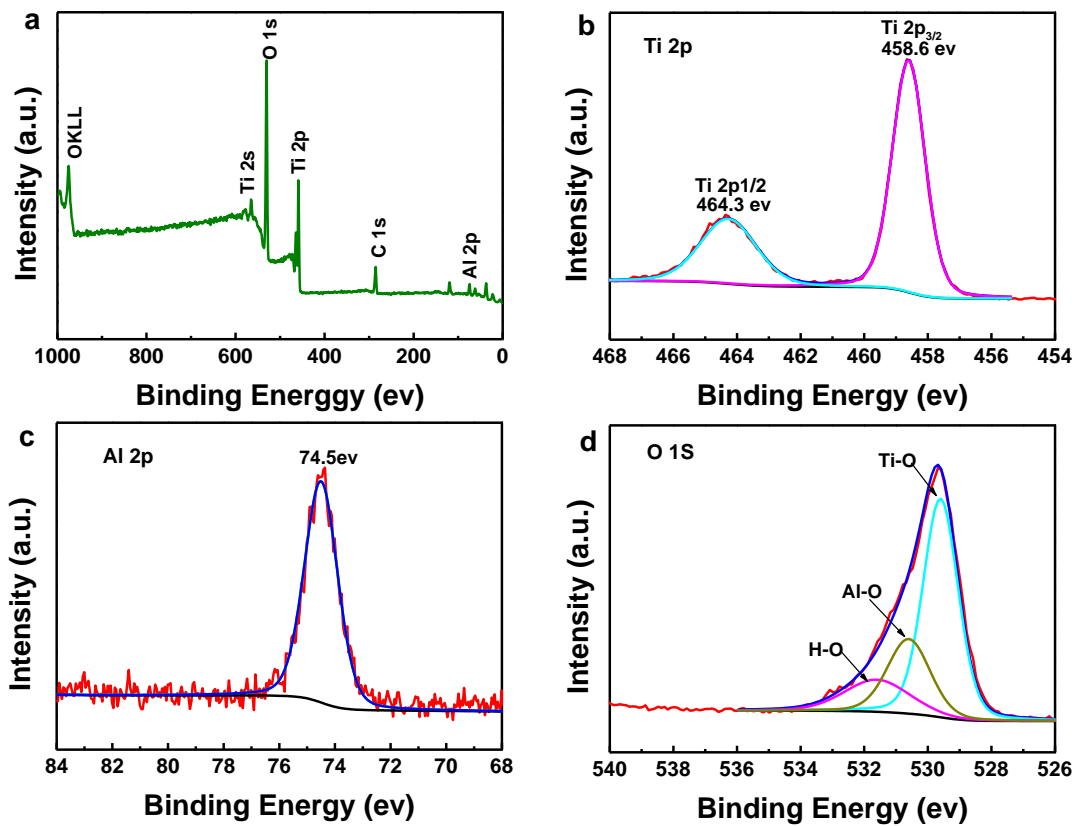


Fig.S1 (a) The XPS spectrum of ALTO, and (b) Ti 2p and (c)Al 2p and (d) O 1s spectra of ALTO.

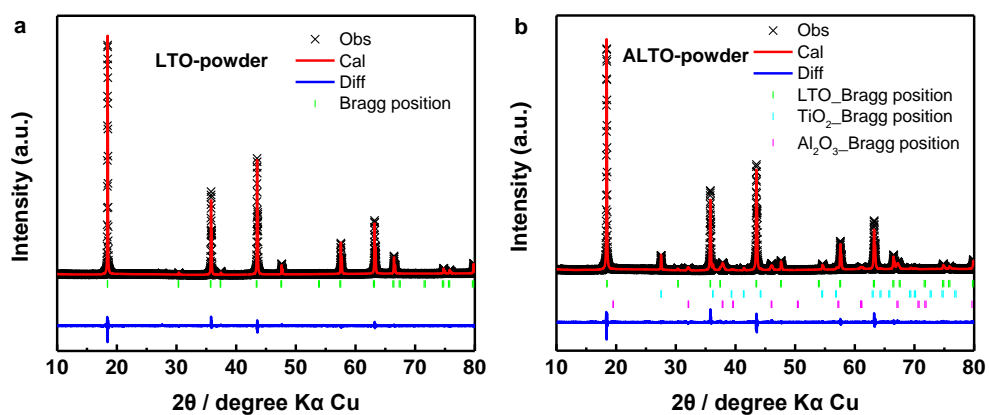


Fig. S2 Rietveld refinement patterns of the LTO powder (a) and the ALTO powder (b).

Table S1. Structural parameters of the LTO and ALTO crystals

sample	a / nm	Volume / nm <sup>3</sup>	Rwp	Rp	$\chi^2$
LTO	8.339(2)	579.919	5.73%	4.29%	3.895
ALTO	8.326(2)	577.209	6.02%	4.64%	3.17

Table S2. The mass percentage of each phase in ALTO powder

Phase	ALTO	rutile-TiO <sub>2</sub>	Al <sub>2</sub> O <sub>3</sub>
Weight Fraction (%)	76.615%	5.3357%	18.049%

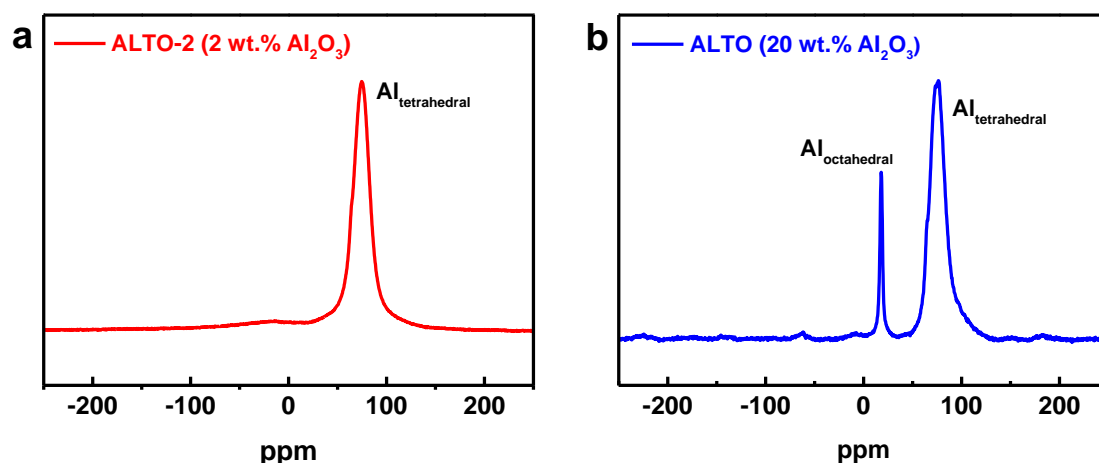


Fig.S3  $^{27}\text{Al}$  MAS NMR spectra of ALTO-2 (2 wt%  $\text{Al}_2\text{O}_3$ ) (a) and ALTO (b). Isotropic peaks at around 74 and 17 ppm are attributed to  $\text{Al}^{3+}$  ions in the tetrahedron ( $\text{AlO}_4$ ) and the octahedron ( $\text{AlO}_6$ ), respectively. The ALTO-2 was synthesized by a solid-state reaction by using  $\text{Li}_4\text{Ti}_5\text{O}_{12}$  and nano- $\text{Al}_2\text{O}_3$  with a weight ratio of 49:1, in which the precursors were ground thoroughly and then calcined at 800 °C for 24 h in air.

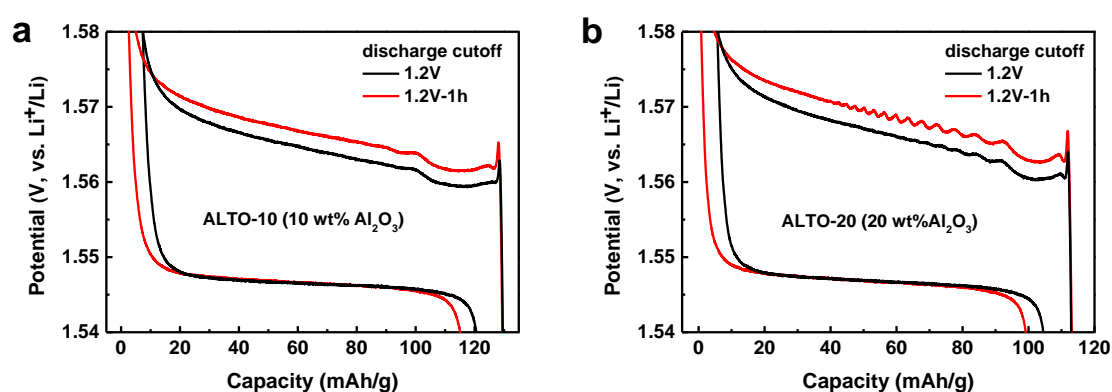


Fig.S4 Two discharge/charge cycles of Al-doped  $\text{Li}_4\text{Ti}_5\text{O}_{12}$  composites with the first cycle as discharge to 1.2V and charge to 2V (black curve), and the second cycle as discharge to 1.2V, potentiostatic for 1 h and charge to 2V (red curve). The Al-doped  $\text{Li}_4\text{Ti}_5\text{O}_{12}$  composites were synthesized by a solid-state reaction by using LTO and nano- $\text{Al}_2\text{O}_3$  with a weight ratio of 4:1 (a) and 9:1(b), in which the precursors were ground thoroughly and then calcined at 800 °C for 24 h in vacuum.

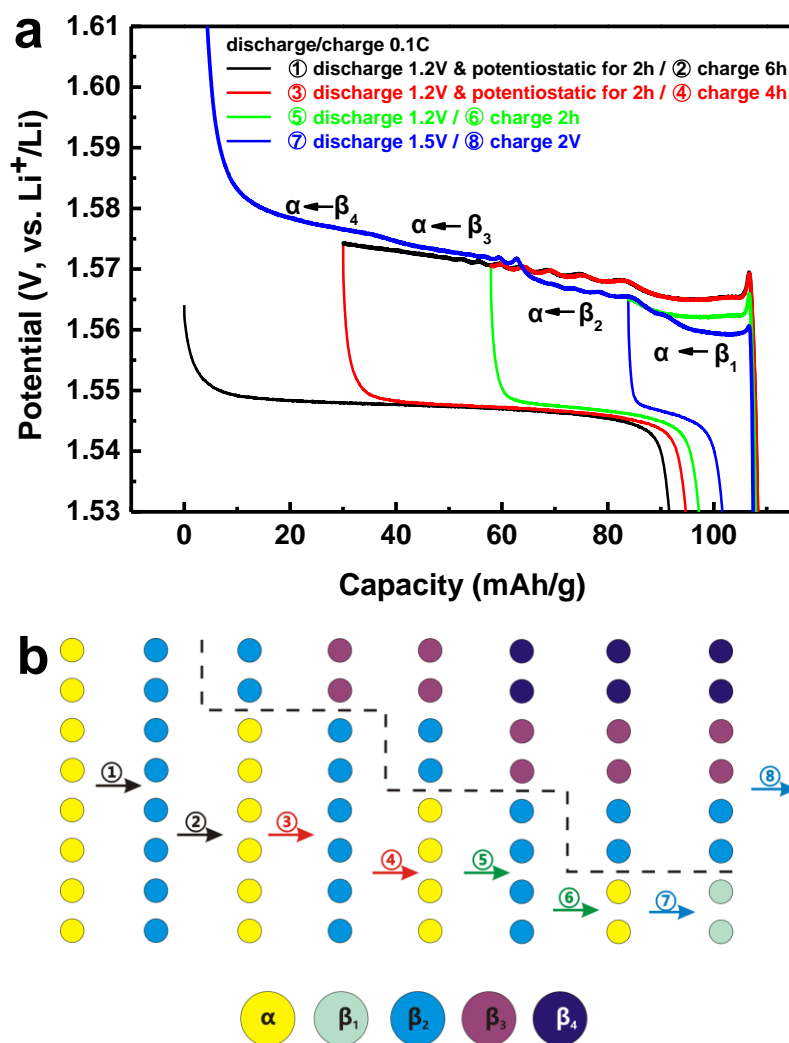


Fig.S5 (a) The dependence of the electrochemical oscillation on the memory effect in ALTO. A sequence of four cycles: (1) discharge to 1.2 V and potentiostatic for 2 h, and charge for 6 h (black curve). (2) discharge to 1.2 V and potentiostatic for 2 h, and charge for 4 h (red curve). (3) discharge to 1.2 V, and charge for 2 h (green curve). (4) discharge to 1.5 V, and charge to 2 V (blue curve). The current rate is 0.1 C. (b) Schematic diagram of phase transitions in ALTO under different discharging cutoffs, in which  $\alpha$  is the delithiated phase,  $\beta_1$  is the lithiated phase, and  $\beta_2$ ,  $\beta_3$ ,  $\beta_4$  is the lithiated phase discharged to a very low cutoff potential.

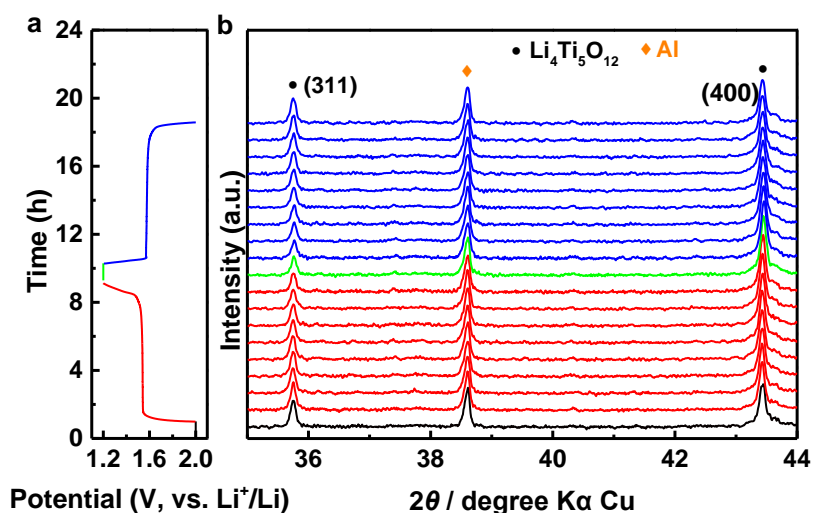


Fig.S6 In situ characterization of ALTO electrode. (a) The following electrochemical measurements were performed: potentiostatic at 2 V for 1 h (black line), discharging to 1.2 V at 0.1 C (red line), potentiostatic at 1.2 V for 1 h (green line), charging to 2 V at 0.1 C (blue line).(b) In situ X-ray diffraction (XRD) patterns during the charge and discharge processes.

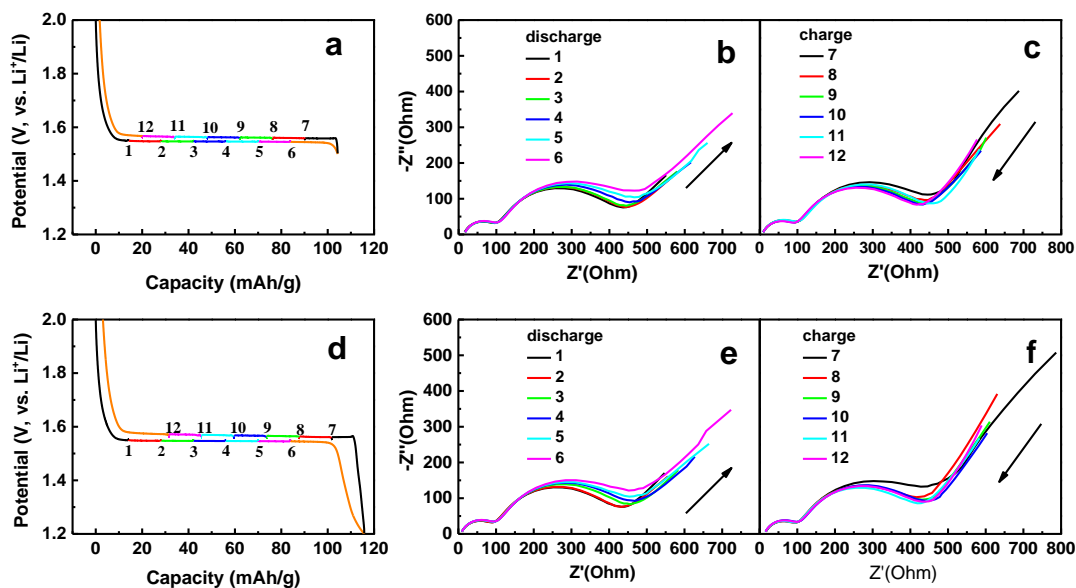


Fig.S7 The charge - discharge curve at a current of 0.1 C for ALTO at (a, d) different discharging cutoffs (1.5V and 1.2V, respectively), in which the cell was switched off every hour for EIS measurement with one hour relaxation. The EIS spectra of ALTO were measured over the range of  $10^6$  Hz to  $10^{-2}$  Hz at different states of (b, e) charge and (c, f) discharge in the two-phase region.

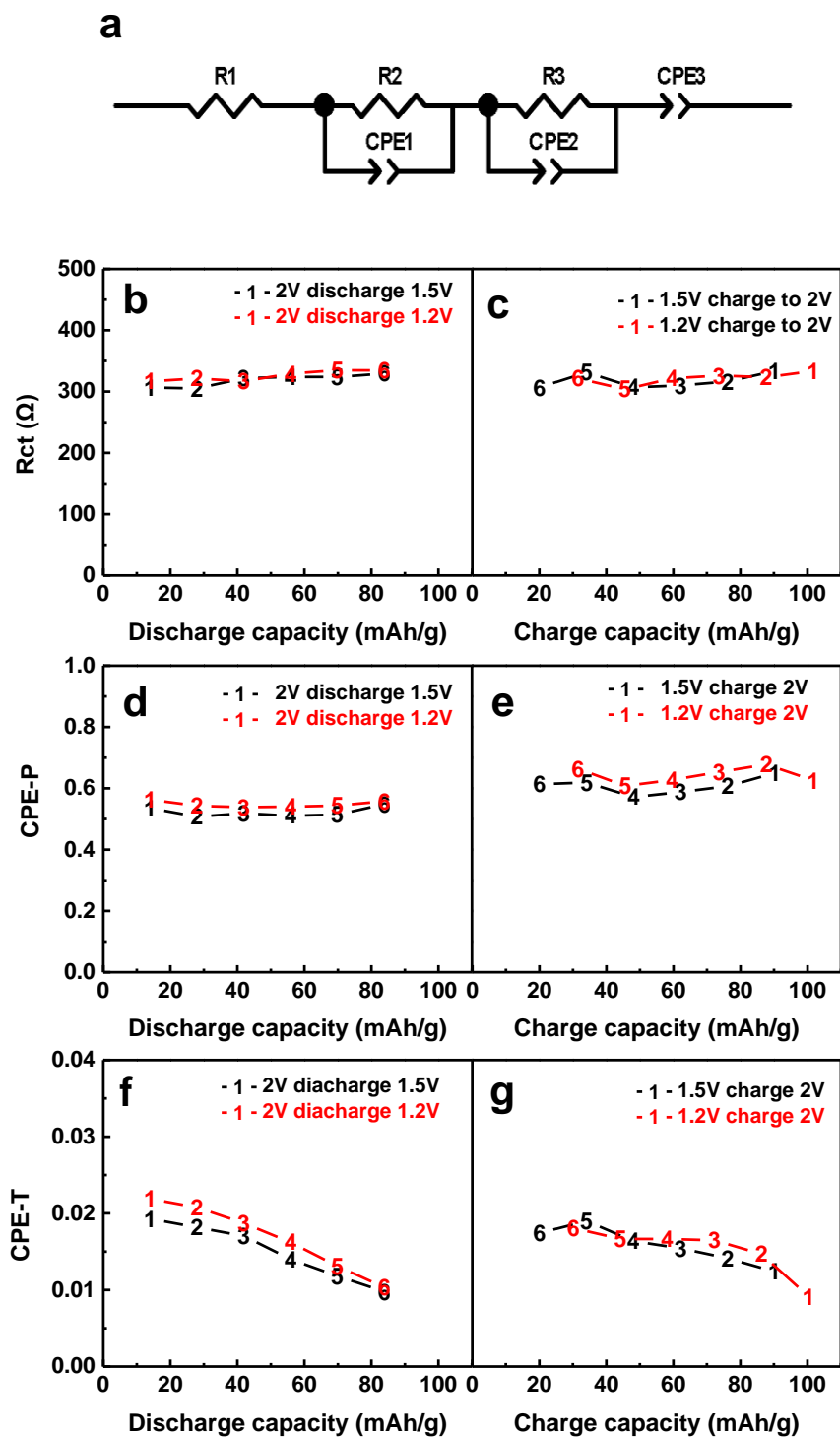


Fig.S8 (a) A Randle equivalent circuit to simulate the impedance spectra of ALTO electrode. The simulated Rct ( $R_3$ ) values of (b) discharge process with different cut off (black, 1.2V; red, 1.5V) and (c) charge process. The simulated CPE-P and CPE-T ( $CPE_3$ ) values of the discharge process (d, f) with different cut off (black, 1.2V; red, 1.5V), and the charge process (e, g).

## References

1. D. Li, X. Liu and H. Zhou, *Energy Technology*, 2014, **2**, 542-547.
2. Y. Shi, L. Wen, F. Li and H.-M. Cheng, *Journal of Power Sources*, 2011, **196**, 8610-8617.
3. J. Zai, Y. Liu, X. Li, Z.-f. Ma, R. Qi and X. Qian, *Nano-Micro Letters*, 2017, **9**, 21.
4. Y. Gao, M. Nagai, Y. Masuda, F. Sato, W. Seo and K. Koumoto, *Langmuir*, 2006, **22**, 3521-3527.
5. J. F. Moulder, W. F. Stickle, P. E. Sobol and K. D. Bomben, *Physical Electronics Division, Perkin-Elmer Corporation*, 1992, 84-85.
6. C.-a. Zhou, X. Xia, Y. Wang, Y. Zhong, Z. Yao, X. Wang and J. Tu, *Journal of Materials Chemistry A*, 2017, **5**, 1394-1399.
7. T. Xia, W. Zhang, J. B. Murowchick, G. Liu and X. Chen, *Advanced Energy Materials*, 2013, **3**, 1516-1523.
8. E. S. Blaakmeer, F. Rosciano and E. R. H. van Eck, *The Journal of Physical Chemistry C*, 2015, **119**, 7565-7577.
9. K. Nakamura, K. Shimokita, Y. Sakamoto, K. Koyama, T. Moriga, N. Kuwata, Y. Iwai and J. Kawamura, *Solid State Ionics*, 2018, **317**, 214-220.
10. B. Tu, H. Zhang, H. Wang, W. Wang and Z. Fu, *Inorganic chemistry*, 2018, **57**, 8390-8395.
11. D. Li, Y. Sun, X. Liu, R. Peng and H. Zhou, *Chem Science*, 2015, **6**, 4066-4070.